Proceedings of the 4th International Conference on Machine Learning and Automation
DOI: 10.54254/2755-2721/2026.36456

Full-Field Wave Height Prediction and Closed-Loop Wave-Making Control Method Based on Binocular Vision and Deep Learning

Ruichang Liu

College of Engineering, Ocean University of China, Qingdao, China
13545905666@163.com

Abstract. Contact-type wave gauges in closed-loop wave-making control cannot obtain the entire field of wave information, and binocular stereo matching is also unreliable on weakly textured water surfaces. A binocular vision-based wave measurement method has been proposed in this paper, and near-infrared speckle projection, HDR imaging, deep-learning regression, geometric stereo matching, etc., have been combined; a closed-loop wave-making control strategy has also been proposed. Integrate the adjustment of the ResNet50-based wave-height regression model and geometric depth estimation for whole-field measurement of wave height. Bi-level optimisation can be employed, and then MIMO PID control, cubic spline interpolation and S-curve motion profiles can be used to develop a controller for controlling the regulation of the eight wave-making units in smooth waveform switching. In a 50m×30m×3m wave basin, during the experiment, the steady-state wave-height tracking RMSE was 0.38mm, the response time was 0.6s, and the post-switching deviation was less than 0.5mm. The new method will be more precise and timely in tracking the change in the height of the waves to improve the stability of high-definition wave-making control operation.

Keywords: binocular stereo vision, wave measurement, deep learning, graph-cut matching, closed-loop wave-making control

1. Introduction

Wave-making technology provides the basis for ocean engineering experiments, the hydrodynamic analysis of ships and other marine-related studies, etc [1]. The conventional type of wave gauge is a contact type, and a PID controller is used; however, a single measurement point may be disturbed by the flow field and fails to provide complete wave information. Stereo vision is a non-contact way to obtain the whole-field waveform. Since it was first mentioned by Benetazzo [2], vision-based wave measurement has been realised through the WASS platform [3] and subsequently studied in the following years [4]. Weak surface texture, specular reflection and cumulative errors in the stereo matching-depth recovery pipeline are still problems of the measurement accuracy of traditional methods such as SGBM [5] and SIFT-based approaches [6, 7].

© 2026 The Authors. This is an open access article distributed under the terms of the Creative Commons Attribution License 4.0 (https://creativecommons.org/licenses/by/4.0/).

DOI: 10.54254/2755-2721/2026.36456

At present, the wave measurement method that has been applied is active texture enhancement [8-11] or passive stereo matching optimisation [12, 13]. Active methods can improve the characteristics of images with artificial tracers, but there will be water contamination and uneven distribution of particles; passive methods can improve disparity estimation, but they are also very sensitive to the quality of stereo matching. Recently, some progress has been made in deep-learning-based stereo matching methods; for example, TSAR-MVS [12], Fast Stereo Conformer [13] and sparse-diffusion stereo matching [14, 15] an accurately reconstruct images even when there is a lack of texture. RAFT-Stereo [16] and deep-learning-based wave run-up recognition [16] have also been achieved in the field of learning-based methods for wave measurement. However, most of the current research is still based on the indirect stereo matching-depth estimation framework and primarily uses open-loop measurement; there has been little attention to integrated closed-loop wave-making control.

The problems listed above can be solved by the means of full-field wave-height measurement in this paper, and near-infrared speckle projection, HDR imaging, deep-learning-based wave-height regression and geometric stereo matching based on binocular vision will be used together. The two ways are a double-path fusion structure and a geometrically constrained stereo reconstruction that have good stability and accuracy in the measurement. Based on the above, a closed-loop wave-making control framework consisting of bi-level optimisation and MIMO PID control has been constructed to achieve coordinated regulation of the eight independent wave-making units. According to the experimental results in a 50m×30m×3m wave basin, the system is capable of providing accurate wave-height data, has stable steady-state tracking performance, smooth waveform transition, and is more suitable for engineering application than the conventional method.

2. Closed-loop wave-making control method based on improved binocular wave height measurement

The general structure of the closed-loop wave-making control system in this paper is shown in Figure 1. First, a good quality stereo image pair is obtained by combining near-infrared speckle projection and HDR imaging. The two figures above are used to get the total wave height by means of deep learning regression and geometric stereo matching. Then the fused wave-height field is taken as the input to bi-level optimisation and MIMO PID control to close the regulation loop.

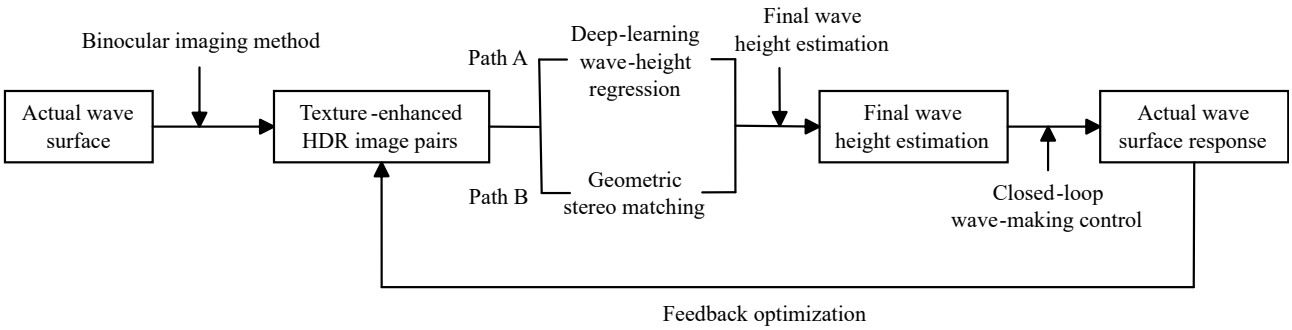


Figure 1. Flowchart of the closed-loop wave-making control method

2.1. Binocular imaging method

A couple of eyes can gather some relatively stable wave-height data. The parts of the near-infrared speckle projection system are adaptive exposure control, HDR imaging, polarisation filter, stereo

DOI: 10.54254/2755-2721/2026.36456

rectification, etc. As shown in Figure 2, the whole imaging workflow can produce good stereo image pairs for wave height calculation.

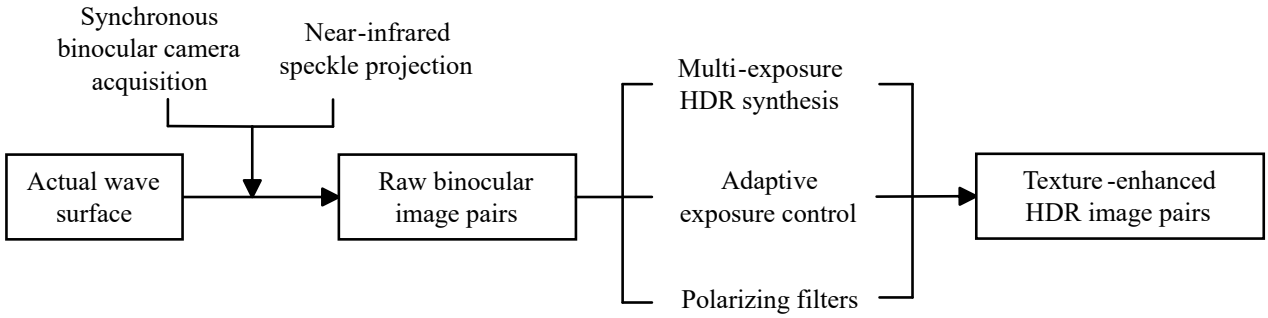


Figure 2. Flowchart of the binocular imaging method

The above problems are weak texture of the water surface and unstable feature extraction. To solve the above problems, at present, random speckle patterns can be formed on the surface of water by an 850 nm near-infrared laser. The resulting speckles have irregular shapes, are in the range of 0.3-0.8 mm, and the density of feature points is about 40-100 points/cm^2. Take some more pictures or use High Dynamic Range to reduce the specular highlight and shadow occlusion. In the normal closed-loop mode, both of the dual-exposure times are 5ms and 15ms, and they can meet the 30Hz sampling requirement. If it is too dark, add a third 45ms exposure to have a total of three exposures in the HDR composite. It has a high switching frequency of 90 Hz, so only one short-exposure image needs to be acquired to meet the speed demand. Get the RAW image, convert it to a linear radiometric space based on the camera response function, and then add Gaussian weight to give more weight to moderately exposed areas and reduce both underexposed and overexposed pixels.

Adjust the exposure control routine to account for the different light conditions of the left and right views, as they are viewed at different angles. In each cycle, the average luminance values of the left and right images, LL and LR, and their difference ΔL are calculated. If $\Delta L > 10$, then set the exposure parameters according to the ratio k = ($L_{current}$- 128) / 128. Repeat the above step several times until the difference in grayscale values of the two stereo images is smaller than the upper limit. A Polarising Filter can reduce the size of the specular reflection and improve the photometric uniformity of the two images.

2.2. Wave height measurement method based on multi-source weighted fusion

The stereo matching pipeline in the conventional binocular wave measurement method has errors. Therefore, a two-channel system will be employed to solve the problem mentioned above. Path A is a deep learning model based on ResNet50 that directly predicts the wave-height field, and Path B reconstructs the geometric depth by means of optical-flow deblurring and then graph-cut stereo matching. Choose the results of the two paths according to different circumstances to obtain a general estimate of wave height.

(1) Path A: Deep-Learning Regression

Path A is a regressor network that directly predicts the wave-height field from rectified stereo image pairs.

The three levels of the network are feature extraction, feature fusion and height regression. First of all, ResNet50 is used as the backbone to extract multi-scale features from both the left and right

DOI: 10.54254/2755-2721/2026.36456

images. A matching cost volume is then constructed, and the correspondence between the left and right features is represented by cosine similarity.

Add several heads of self-attention to improve the feature representation of wave crests, troughs and weak-texture areas. Feature fusion and regression computation are carried out to obtain the network's direct output of the water-surface height field. The first two terms of the total loss function are mean squared error and weight regularization

$$L=\frac{1}{N}\sum_{i=1}^{N}(H_{pred,i}-H_{gt,i})^2+\lambda\|W\|^2 \tag{1}$$

The network parameters are optimised by means of the joint loss in Equation (1).

(2) Path B: Geometric Stereo Matching

Path B is the previous geometric stereo matching workflow, and then optical-flow deburring and graph-cut optimisation are added to carry out depth reconstruction.

Fast-moving waves during the exposure time will be blurred due to motion blur and thus lose the precision of stereo matching. To solve the above problem, an image degradation model is proposed as B = I * K + n, where B is the blurred image, I is the latent sharp image, and K is the point spread function. Then, to obtain the sharp image, one can minimise an energy function.

Debarring is done, and then graph cuts are employed for stereo matching. Assign a disparity label $f_p \in \{0, 1, ..., dmax\}$ to each pixel p, and then minimise the energy function in Equation (2) to obtain the globally optimal disparity map.

$$E(f)=\sum_{p\in P}D_p(f_p)+\sum_{(p,q)\in N}V_{p,q}(f_p,f_q) \tag{2}$$

Finally, the disparity map is used for triangulation to obtain 3D depth, and then this is used as input for the next fusion.

(3) Multi-Source Weighted Fusion

The output of Path A and the output of Path B are combined according to the local clarity of the image and disparity confidence indicators, as shown in Equation (3).

$$H_{accurate}=w_{model}\cdot H_{predict}+w_{disparity}\cdot H_{depth} \tag{3}$$

2.3. Closed-loop wave-making control method

Closed-loop wave control should have a small error in wave height and not be noisy. Optimisation and bi-level MIMO PID control with smooth waveform switching are employed in the hierarchical control. As shown in Figure 3, the estimated full-field wave-height error is first used to determine how much displacement of the wave-box and servo speed are required in the bi-level optimisation model. The above commands will then be carried out one by one by the eight wave-making units through MIMO PID control. At the same time, cubic spline interpolation is used to connect the start and end points of S-curve acceleration and deceleration smoothly.

(1) Bi-Level Optimization Model

DOI: 10.54254/2755-2721/2026.36456

The old PID controller has fixed weights and cannot be used in the wave-making system. Therefore, a two-stage optimisation framework in the Stackelberg game model is put forward. The upper level reduces the amplitude and phase error of the wave box to obtain the desired displacement of the wave box, and the lower level minimises mechanical vibration energy and displacement tracking error to adjust the speed of the servo motor. The two levels will iterate and exchange control variables until they converge, then adjust the precision of wave generation and vibration suppression together. The upper-level objective function is given by Equation (4).

$$F_{upper}=\frac{\|H_{error}\|^2}{H_{target}\times\sqrt{H_{target}}}+\frac{|\phi_{error}|}{T_{target}}\times\frac{n_{motor}^2}{n_{rated}^2} \tag{4}$$

The objective function of the lower-level execution model in the bi-level game optimisation structure is given by Equation (5).

$$F_{lower}=\frac{a_{stroke}^2}{a_{max}^2}+\frac{\omega_{plate}^2}{\omega_{max}^2}-\frac{|d_{desired}-d_{actual}|}{A_{max}}\times\frac{n_{motor}}{n_{rated}} \tag{5}$$

(2) MIMO PID Controller

Given that the distributions of hydrodynamic forces for the eight independent wave-making units are all different, a MIMO PID control method will be employed. The control path of each unit is different, and according to optimisation based on the Ziegler-Nichols method and experimental response characteristics, it can be started up. According to the theory of Airy waves, to improve the dynamic tracking performance, a feedforward compensation term can be added to the PID feedback loop to correct for any remaining tracking error. The control cycle is 50ms and it is in sync with the binocular vision measurement system. The control output for wave-making unit i is given by Equation (6).

$$\Delta n_i(t)=K_{p,i}\cdot e_i(t)+K_{i,i}\cdot\int_0^t e_i(\tau)d\tau+K_{d,i}\cdot\frac{de_i(t)}{dt} \tag{6}$$

(3) Smooth Waveform Transitions

Mechanical shock and transient fluid oscillations during waveform switching are prevented through a smooth transition method that combines cubic spline interpolation with S-curve motion profiles. Cubic splines generate continuous trajectories linking the current waveform to the target waveform, while S-curve acceleration and deceleration profiles reduce impact loads and improve actuator stability. The transition duration is adjusted adaptively based on the magnitude of the waveform change. Visual feedback from the wave-height measurement system monitors the steady-state condition, allowing rapid and smooth switching between operating states. The number of interpolation nodes is determined from the period difference, and a cubic polynomial is formulated at each node as expressed in Equation (7). $N=10+5\cdot\frac{|T_{target}-T_{current}|}{0.1}$

DOI: 10.54254/2755-2721/2026.36456

$$S_j(t)=a_j+b_j\cdot(t-t_j)+c_j\cdot(t-t_j)^2+d_j\cdot(t-t_j)^3, \quad (t_j\leq t<t_{j+1}) \tag{7}$$

By means of bi-level optimisation, MIMO PID co

ntrol and smooth waveform switching have been employed to develop a new control scheme that can maintain the stable and accurate operation of the multi-unit wave-making system in a closed loop.

3. Wave basin experimental validation and performance evaluation

To know if the proposed all-field wave height measurement and closed-loop wave-making control plan can follow and adjust to the waveform of steady-state waves, experiments were carried out. The former is to check the steady-state value and response speed; the latter is to verify whether the cubic spline interpolation and S-curve motion control can ensure a smooth shape of the waveform.

3.1. Experimental apparatus and calibration

To reduce the interference of wall reflection, passive wave absorbers were added to a 50m×30m×3m indoor wave basin, and then experiments were carried out. The four modules of the experimental system are the double-lens imaging circuit, the near-infrared structured-light projector, a wavemaker and the control computer. The position of the binocular imaging subsystem is 4.5 metres from the wavemaker, and it has been set up with two synchronous industrial cameras, an 800mm baseline, a resolution of 640x480 pixels, 16mm focal-length lenses and a maximum sampling rate of 90Hz. A structured-light projector was used to produce random speckles (0.3-0.8 mm, 40-100 points/cm^2) in the 850 nm, 500 mW semiconductor laser via a ground-glass diffuser, and this light covered an area of 1.2-1.5 m in front of the wavemaker. There are 8 piston-type modules of the wavemaker, and they are driven by a 2.2kW AC servo motor at 3000 rpm. A coupling-ball screw-nut housing-connector transmission is used to convert the rotary motion into linear motion, and the maximum wave-box stroke is 120 mm. The general shape and way of transmission are shown in Figs. 3 and 4.

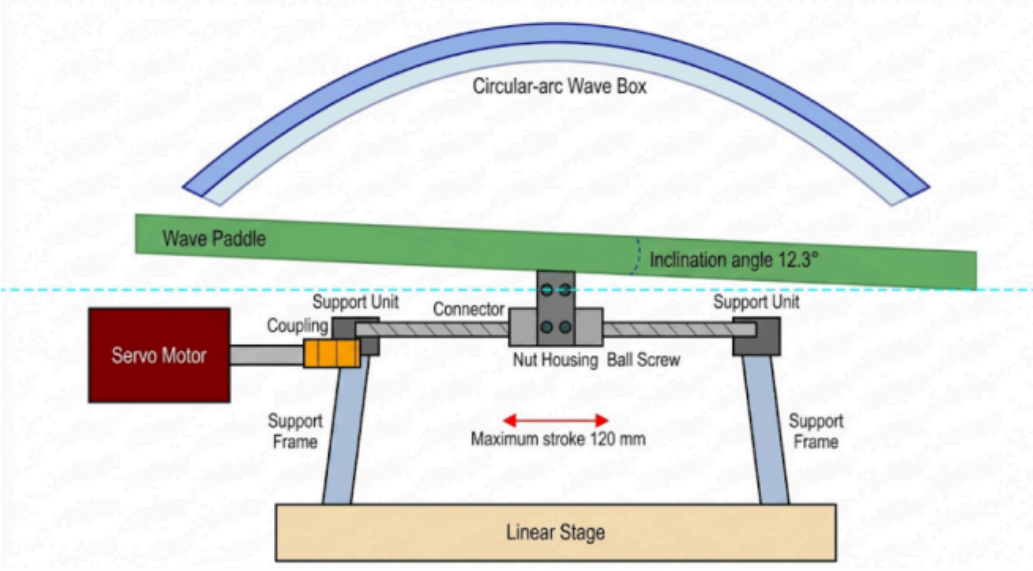


Figure 3. Schematic diagram of the overall structure of the wave-making unit

DOI: 10.54254/2755-2721/2026.36456

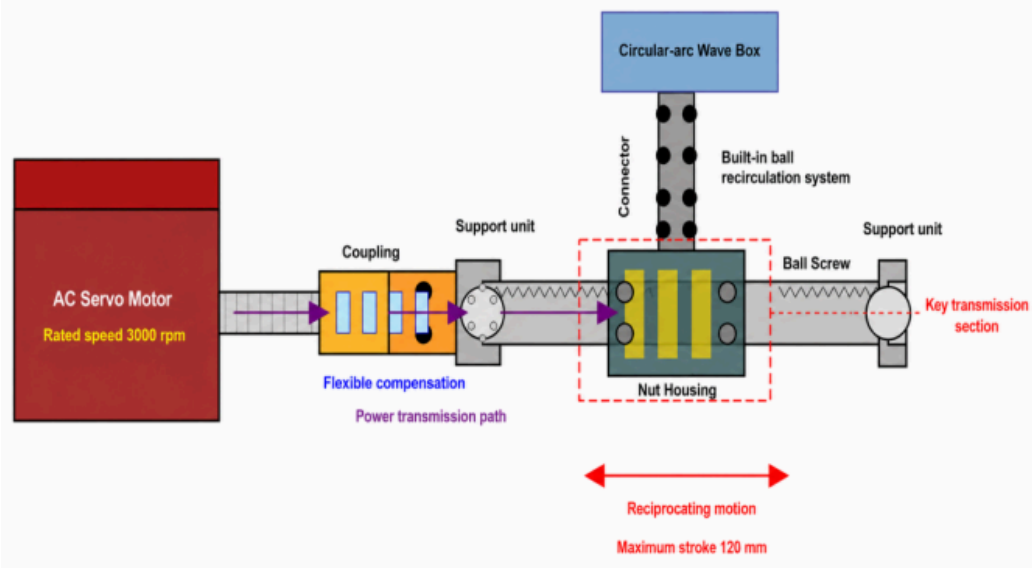


Figure 4. Partial view of the transmission system of the wave-making unit

Zhang's method has been employed for the calibration of the binocular system to improve the accuracy of wave-height measurement and 3D reconstruction. Fifteen pairs of images were obtained from a 20mm x 20mm checkerboard to obtain the internal and external parameters of the camera. As shown in Figure 6, the difference in focal length of the two cameras is less than 0.5%, the relative rotation angle is less than 0.5°, the baseline error is 1.7 mm, and the mean reprojection error is 0.28 pixels. Adaptive Exposure Control has reduced the difference in brightness of the two sets of stereo images by 14 grayscale levels to 4, and it can now be used for stereo matching and wave-height estimation.

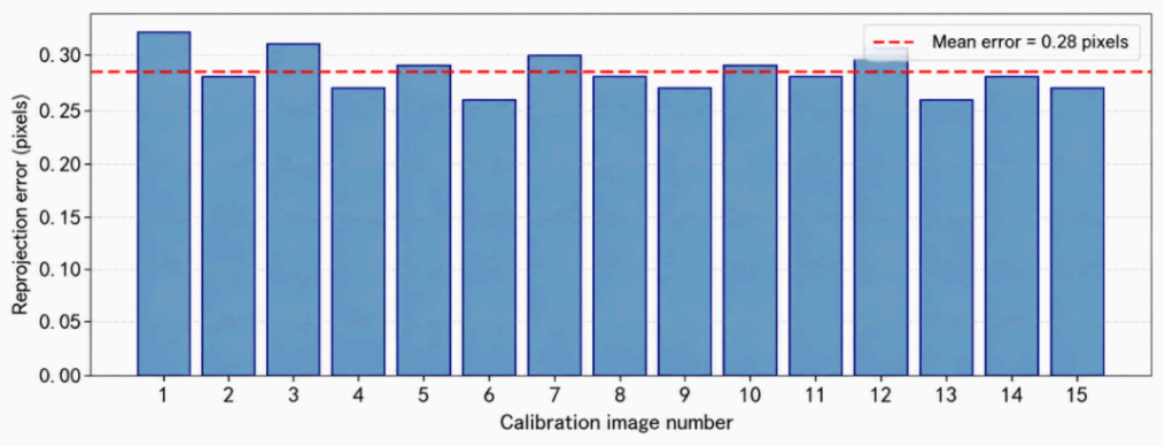


Figure 5. Distribution of reprojection errors in binocular imaging system calibration

3.2. Steady-state tracking experiments via wave height regression training

Target waves for the eight situations in Table 1 have been created. Gather a total of 72,000 stereo image pairs over a period of 300 seconds at a frame rate of 30Hz, and then divide them into a training set and a test set in an 8:2 ratio. Data augmentation consists of random rotation (±5°), scaling (0.9-1.1), luminance adjustment (0.8-1.2) and Gaussian noise (σ = 5 grayscale levels), and it was used at the same time as the epipolar constraint. Adam optimizer will be employed to train the

DOI: 10.54254/2755-2721/2026.36456

model, set the learning rate to 0.001 and the batch size to 32; cosine annealing and early stopping will also be applied. It took about 18 hours to train one NVIDIA RTX 3090 GPU for 200 epochs.

Table 1. Wave parameters of the wave height regression model training dataset

Waveform No.	Wave Height (mm)	Period (s)	Wavelength (m)	Sample Size
1	50	1.0	1.56	9000
2	80	1.2	2.25	9000
3	120	1.5	3.51	9000
4	160	1.8	5.06	9000
5	200	2.1	6.88	9000
6	240	2.5	9.76	9000
7	280	2.8	12.23	9000
8	300	3.0	14.04	9000

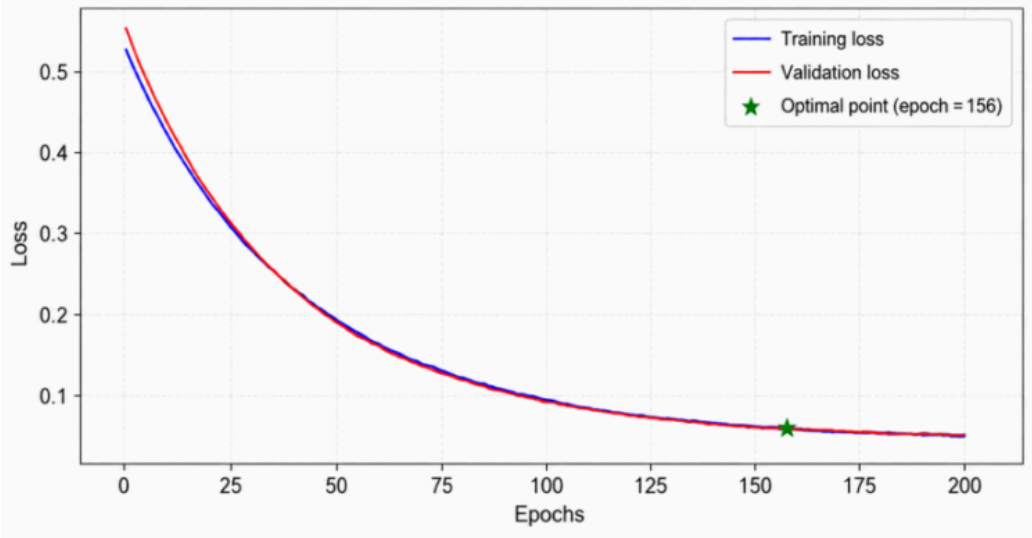


Figure 6. Training and validation loss curves of the wave height regression model

To know if the closed-loop control system is working normally, a tracking test will be conducted with a sine wave having a reference amplitude of 150mm and a period of 2.0s. Based on the wave-height data, a system was constructed to reduce the initial wave-height error of 7.83 mm and the phase error of 0.12 rad to less than 0.6 seconds of steady-state time. At the steady state, the RMSE of the wave-height tracking was 0.38mm (0.25% of the target amplitude), the standard deviation was 0.35mm, the maximum error was 2.8mm, and the phase error was less than 0.04rad. Figure 8 is a reconstructed wave-height field and Figure 9 is the comparison of the measured and target wave surfaces.

DOI: 10.54254/2755-2721/2026.36456

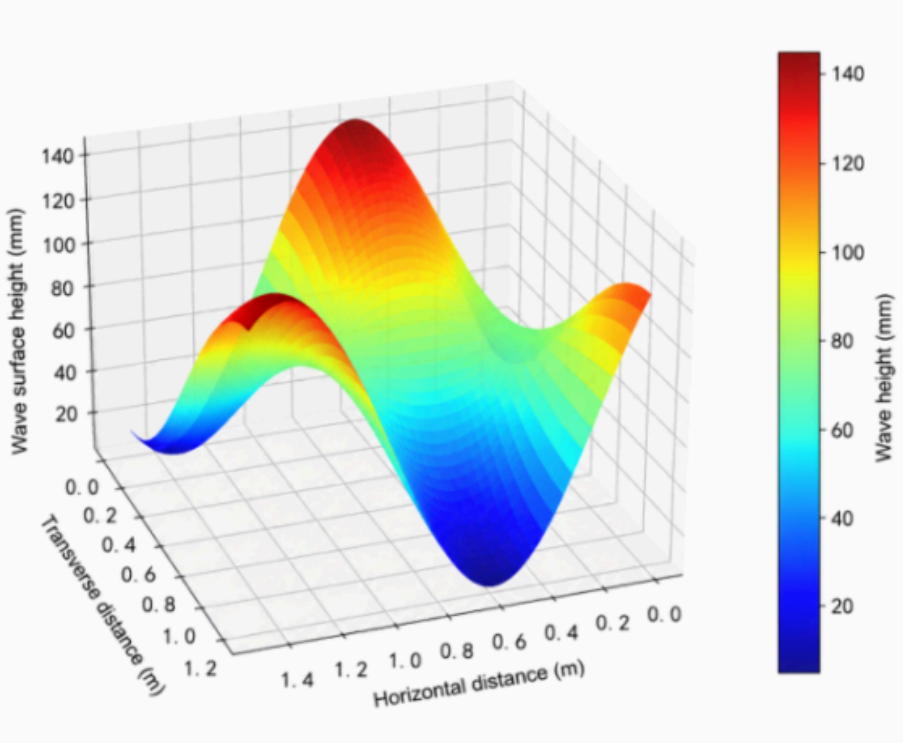


Figure 7. Precise 3D visual reconstruction of the water surface height field

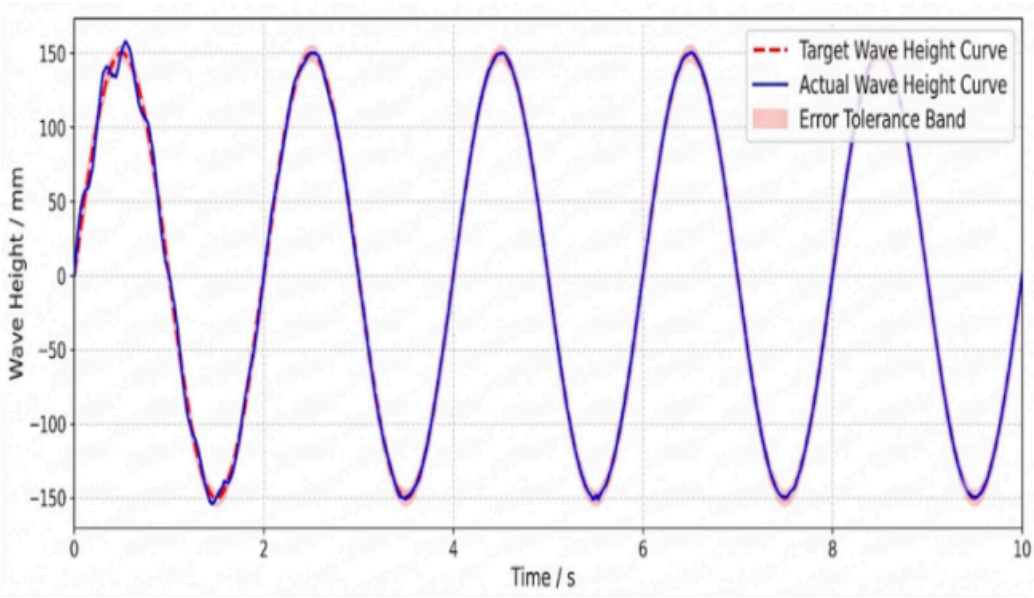


Figure 8. Curves of the actual and target water surface height during closed-loop control

3.3. Waveform transition experiment

To test the proposed cubic spline interpolation and S-curve motion plan, the target waveform was modified; that is, after 180 seconds of continuous operation, both the amplitude and period were increased from 150 mm and 2.0 s to 200 mm and 2.5 s. A cubic spline will be established with 32 interpolation nodes, and the transition duration and sampling frequency will be set to 12s and 90Hz, respectively. Fig. 10 is the wave height and phase deviation at the time of transition. The maximum

DOI: 10.54254/2755-2721/2026.36456

phase deviation is about 0.34 rad at about 5 s, and at this time, the peak wave-height deviation reaches 19.3 mm. Both deviations gradually approached the S-curve motion control and then stabilized after 12 seconds; at this time, the wave-height deviation was about 7.6 mm and the phase deviation was 0.12 rad.

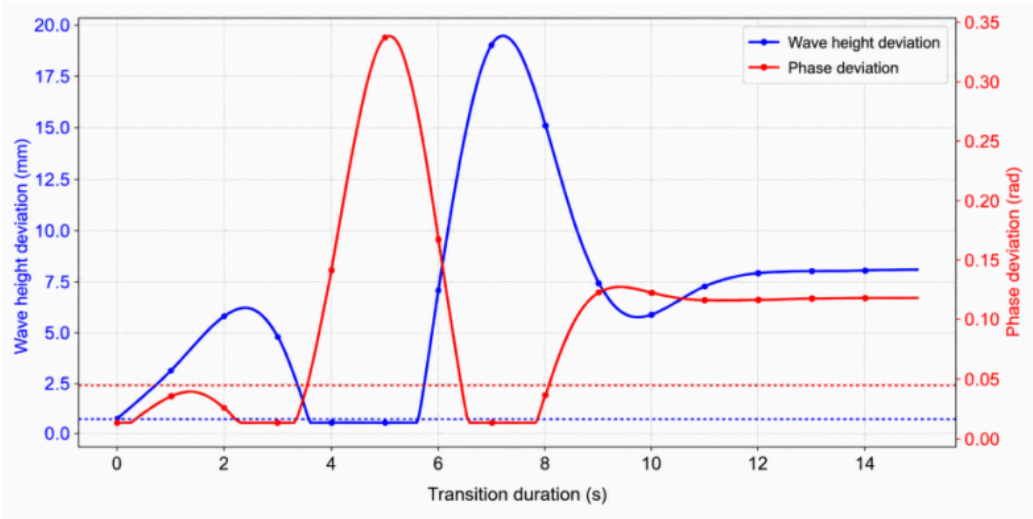


Figure 9. Evolution curves of wave height deviation and phase deviation during waveform transition

4. Method comparison and discussion

The two usual ways for machine vision-based wave measurement have also been adopted in this paper. Most of the previous research has concentrated on the accuracy of measurement and 3D reconstruction, but little attention has been paid to the closed-loop integration of wave-making systems. a 6-DOF motion platform was used for calibration, and only then could surface reconstruction be carried out in the wave flume. Table 2 is a comparison of the experimental situation, measurement range, information fusion and control ability of the above methods. Although the Environments are different, the proposed method can still achieve dual-path wave-surface measurement, multi-source fusion and closed-loop verification in a 50m×30m wave basin to construct an all-encompassing framework for wave perception, state estimation, closed-loop control and smooth waveform transition.

Table 2. Overall Performance Comparison of the Proposed Method and Existing Methods.

Performance Metric	Proposed Method	Ref [10]. (Wu 2024)	Ref [11]. (Wang 2025)
Wave height measurement accuracy	RMSE = 0.38 mm	Error < 5%	Error 3.17%~11.60%
Measurement mode	Full-field 128×96 grid	Sparse 3D feature points	Full-field 3D point cloud
Texture enhancement	850 nm near-infrared speckle	None (Passive)	None (Pure software affine)

DOI: 10.54254/2755-2721/2026.36456

Table 2. (continued)

Depth acquisition	ResNet50 regression + Graph cuts	PSM-Net	Graph cuts + Affine ratio
HDR imaging	Yes (Hierarchical multi-exposure)	No	No
Motion deblurring	Variational optical flow deblurring	Not mentioned	Not mentioned
Closed-loop wave-making control	Yes (Bi-level optimization + MIMO PID)	No	No
Smooth waveform transition	Yes (Spline + S-curve)	No	No
Experimental environment	50 m × 30 m wave basin	6-DOF platform	108 m × 7 m wave flume
Response time	0.6 s	Not mentioned	Not mentioned
Inference time	12 ms/frame	Not mentioned	Not mentioned

4.1. Advantages of the proposed method

The accuracy of the proposed method for wave-height measurement is high (RMSE = 0.38 mm) and its response speed is fast (0.6 s); the four main modules of this method are as follows:

(1) Imaging: The near-infrared window of AirDrum spectroscopy is used, and with the help of HDR imaging and a polarisation filter, the texture of the water surface and specular reflection can be shown.

(2) Measurement: The two-path fusion framework is a kind of deep-learning regression and geometric stereo matching method that can use the semantic robustness of weak-texture areas and the geometric accuracy of texture-rich areas.

(3) Control: A two-tier optimisation model is employed to regulate the wave-height tracking and vibration suppression simultaneously, and then MIMO PID control is used to accurately adjust the number of units.

(4) Execution: Cubic spline interpolation and S-curve motion planning can be used to reduce the fluctuation of the waveform and mitigate transient vibration. The above parts together form a 50ms closed-loop control cycle that can coordinate perception, control and actuation.

4.2. Limitations

Only one normal sine wave has been tested so far of the proposed method. Validation under irregular waves (e.g., JONSWAP spectrum), multidirectional waves, breaking waves, long-range measurements (>5 m), outdoor illumination variations and long-term continuous operation (>24 h) have not been carried out. A wave-height regression model was also trained on the data in which the wave height was between 50-300 mm and the wave period was between 1.0-3.0 s. It needs to be confirmed that it generalizes well outside the training set.

DOI: 10.54254/2755-2721/2026.36456

5. Conclusions

A wave-surface measurement method has been developed in this paper to combine near-infrared speckle enhancement, HDR imaging, deep-learning-based wave-height regression and geometric stereo matching to solve the problem of full-field wave-height measurement for closed-loop wavemaker control. A closed-loop control scheme based on bi-level optimisation and MIMO PID control has been put forward. Based on the experiments conducted in the usual wave conditions, the key results are summarized below.

(1) An imaging framework that combines near-infrared active texture enhancement with multi-source image optimization substantially improved the visibility of water-surface features and the stability of imaging. The binocular calibration yielded a reprojection error of 0.28 pixels.

(2) A dual-path wave-height measurement framework that fuses deep-learning regression with stereo reconstruction via adaptive weighting achieved millimeter-level accuracy. In large-scale wave-basin experiments, the closed-loop system attained a steady-state wave-height tracking RMSE of 0.38 mm with a response time of 0.6 s.

(3) A closed-loop control strategy incorporating bi-level optimization and MIMO PID control enabled coordinated regulation across multiple wave-making units while maintaining a balance between wave-height tracking precision and vibration suppression.

(4) A smooth waveform-transition strategy based on cubic spline interpolation and S-curve motion planning effectively lowered transient deviations and enhanced switching stability.

The above way has been tested in the large wave basin under normal sinusoidal wave conditions. In the future, research will be expanded to cover irregular, multi-directional and breaking waves; the generalisation ability of the model outside the current training area will be improved, its robustness in all kinds of outdoor light conditions will be verified, and how long it can operate in real engineering applications will also be tested.

References

[1] Swan, C., & Sheikh, R. (2015). The interaction between steep waves and a surface-piercing column. *Philosophical Transactions of the Royal Society A, 373*, 20140114.

[2] Benetazzo, A. (2006). Measurements of short water waves using stereo matched image sequences. *Coastal Engineering, 53*, 1013-1032.

[3] Bergamasco, F., Torsello, A., Sclavo, M., et al. (2017). WASS: An open-source pipeline for 3D stereo reconstruction of ocean waves. *Computers and Geosciences, 107*, 28-36.

[4] Sun, H., Wu, G., Wang, X., et al. (2022). Research on a measurement method for the ocean wave field based on stereo vision. *Applied Sciences, 12*, 7447.

[5] Hirschmuller, H. (2007). Stereo processing by semiglobal matching and mutual information. *IEEE Transactions on Pattern Analysis and Machine Intelligence, 30*, 328-341.

[6] Gomit, G., Chatellier, L., Calluaud, D., David, L., Fréchou, D., Boucheron, R., Perelman, O., & Hubert, C. (2015). Large-scale free surface measurement for the analysis of ship waves in a towing tank. *Experiments in Fluids, 56*, 184.

[7] Caplier, C., Rousseaux, G., Calluaud, D., et al. (2016). Energy distribution in shallow water ship wakes from a spectral analysis of the wave field. *Physics of Fluids, 28*, 107104.

[8] Li, D., Xiao, L., Wei, H., et al. (2022). Spatial-temporal measurement of waves in laboratory based on binocular stereo vision and image processing. *Coastal Engineering, 177*, 104200.

[9] Li, D., Xiao, L., Wei, H. (2024). Real-time reconstruction of wave field in laboratory based on binocular stereo vision. *Journal of Ship Mechanics, 28*(10), 1463-1471.

[10] Wu, J., Chen, S., Liu, S., et al. (2024). Research on wave measurement and simulation experiments of binocular stereo vision based on intelligent feature matching. *Frontiers in Marine Science, 11*, 1508233.

[11] Wang, F., Zhu, Q. (2025). Artificial texture-free measurement: A graph cuts-based stereo vision for 3D wave reconstruction in laboratory. *Journal of Marine Science and Engineering, 13*, 1699.

DOI: 10.54254/2755-2721/2026.36456

[12] Yuan, Z., Cao, J., Wang, Z., et al. (2024). TSAR-MVS: Textureless-aware segmentation and correlative refinement guided multi-view stereo. *Pattern Recognition, 154*, 110565.
[13] Lu, Y., He, X., Zhang, Q., et al. (2025). Fast stereo conformer: Real-time stereo matching with enhanced feature fusion for autonomous driving. *Engineering Applications of Artificial Intelligence, 139*, 109632.
[14] Zhang, L., Cong, W., Sun, L., Liu, Q., Liu, G., & Yang, Y. (2026). A sparse diffusion-based stereo matching algorithm for binocular vision. *Journal of Jilin University (Engineering and Technology Edition)*.
[15] Jebari, O., Weaver, J., Kim, Y., et al. (2025). Wave-field reconstruction using stereo cameras on a floating platform in a synthetic environment. *Ocean Engineering, 323*, 120647.
[16] Shen, Y., Huang, J., Chen, M., Chen, W., & Liu, H. (2026). Recognition and statistical analysis of the temporal process of wave run-up on river embankments based on image deep learning. *Ocean Engineering*.